Preparation of high-performance $Ca_3Co_4O_9$ thermoelectric ceramics produced by a new two-step method

M. A. Madre,[1] F. M. Costa,[2] N. M. Ferreira,[2] A. Sotelo,[1] M. A. Torres,[3] G. Constantinescu,[1] Sh. Rasekh,[1] J. C. Diez[1]

[1]ICMA (CSIC-Universidad de Zaragoza), Dpto. de Ciencia de Materiales, C/María de Luna 3, 50018-Zaragoza (Spain).

[2]i3N, Departamento de Física, Universidade de Aveiro, 3810-193 Aveiro, Portugal.

[3]Universidad de Zaragoza, Dpto. de Ingeniería de Diseño y Fabricación, C/María de Luna 3, 50018-Zaragoza (Spain).

Abstract

High-performance $Ca_3Co_4O_9$ thermoelectric ceramic has been prepared from a $Ca_{1-x}Co_xO/Ca_yCo_{1-y}O$ divorced eutectic structure produced by a directional melt-grown using the laser floating zone technique. This material has been grown at very high solidification rate in order to produce a very fine microstructure to reduce the necessary annealing time to recover the $Ca_3Co_4O_9$ thermoelectric phase as the major one. As-grown and annealed samples were microstructurally characterized to determine the phases and estimate the extent of $Ca_3Co_4O_9$ formation with time and related with their thermoelectric performances. The optimum annealing time, 72 h, has been determined by the maximum power factor value (about 0.42 mW $K^{-2}m^{-1}$), which is around the best values reported in textured materials (~ 0.40 mW $K^{-2}m^{-1}$). This high power factor

outcome from the high $Ca_3Co_4O_9$ phase content, apparent density and Co^{3+}/Co^{4+} relationship determinations performed in the present work.

Keywords: Grain growth; Sintering; Microstructure-final; Electrical properties; Thermopower

* Corresponding author. A. Sotelo

e-mail address: asotelo@unizar.es; Tel.: +34 976762617; Fax: +34 976761957

Introduction

Thermoelectric (TE) materials can transform a temperature gradient to electrical power directly due to the well-known Seebeck effect. The conversion efficiency of such materials is usually quantified by the dimensionless figure of merit ZT, $TS^2/\rho\kappa$ (in which S^2/ρ is also called power factor, PF), where S is the Seebeck coefficient (or thermopower), ρ the electrical resistivity, κ the thermal conductivity, and T is the absolute temperature [1]. This important characteristic has focused attention on this type of materials in order to be applied in practical applications as waste heat recovery devices [2] or solar thermoelectric generators [3]. Furthermore, they can also be used as heating/refrigeration devices [4]. Nowadays, these commercial applications are based on the use of alloys and/or intermetallic thermoelectric materials, such as Bi_2Te_3 or $CoSb_3$, with high thermoelectric performances at relatively low temperatures. On the other hand, these materials posses some drawbacks, as they can be degraded at high temperatures under air and/or releasing toxic or heavy elements. These problems lead to the limitation of their working temperature which reduces their effective performances, as can be deduced from the ZT expression. This temperature limitation was overwhelmed in 1997 by the discovery of attractive thermoelectric properties in the $Na_2Co_2O_4$ ceramic [5]. From the discovery of these properties in that ceramic material, much work has been performed on Co-based materials leading to the discovery of new compositions, such as $[Ca_2CoO_3][CoO_2]_{1.62}$ and $[Bi_{0.87}SrO_2]_2[CoO_2]_{1.82}$ that exhibit promising thermoelectric properties [6-9]. Moreover, these oxide materials have the great advantage of being able to operate at high temperatures in air without degradation, as compared to the intermetallic thermoelectric compounds, which

is another way for improving the ZT values. The crystalline structure of these families has been described as an alternate stacking of two different layers, a common conductive CdI_2-type hexagonal CoO_2 layer with a two-dimensional triangular lattice and a block layer composed, in turn, of insulating rock-salt-type (RS) layers. Both sublattices (RS block and CdI_2-type layer) possess common *a*- and *c*-axis lattice parameters and *β* angles but different *b*-axis length, causing a misfit along the b-direction [10].

It has been demonstrated that the misfit relationship in these materials tailors their thermoelectric performances [9]. As a consequence, many attempts have been made in order to improve their thermoelectric properties via metallic oxides substitution [11-15]. Other works have been focused on the enhancement of grain connectivity and the increase of mechanical properties by metallic Ag additions [16], or by both processes simultaneously [17].

On the other hand, layered cobaltites are characterized by a high anisotropy which leads to the formation of plate-like grains during the crystallization process. This feature can be also exploited in the development of commercial applications for these ceramics, with improved electrical properties, when an adequate grain orientation is produced using texturing techniques. Such grains alignment would allow attaining macroscopic properties comparable to those obtained on single crystals. For these reasons, numerous methods have been studied and reported to be efficient to obtain a good grain alignment, such as spark plasma sintering (SPS) [18,19], sinter-forging [20], template grain growth (TGG) [21], laser floating zone (LFZ) melting technique [22], or the newly reported electrically assisted laser floating zone method (EALFZ) [23].

Previous results on melt-grown layered ceramics have shown that the ceramics produced using the LFZ technique have a very high density (≥ 95 %) [24] which can reduce electrical resistivity and, as a consequence, raising their thermoelectric performances. On the other hand, $Ca_3Co_4O_9$ ceramics produced by the usual solid state sintering methods possess a relatively low density due to the maximum stability temperature of $Ca_3Co_4O_9$ phase (926 ºC), as can be seen in the phase diagram represented in Figure 1 [25], compared with the eutectic point temperature (1350 ºC) which really hinders the densification processes in the sintering step.

The aim of this work is to produce high-quality $Ca_3Co_4O_9$ thermoelectric materials by the new two-step method. This method comprises the LFZ grown of a very fine $Ca_{1-x}Co_xO/Ca_yCo_{1-y}O$ divorced eutectic structure from $Ca_3Co_4O_9$ nominal composition powders, followed by an annealing process at 900 ºC for different time lengths to produce a high density $Ca_3Co_4O_9$ ceramic. It is studied the microstructural and thermoelectric evolution of samples with time. The changes produced on the annealed samples microstructure, compared with the as-grown ones, are correlated with their thermoelectric properties.

Experimental

The initial $Ca_3Co_4O_9$ ceramic powders used in this work have been prepared from commercial $Ca(CH_3CO_2) \cdot 1/2H_2O$ (≥ 99%, Aldrich) and $Co(CH_3CO_2)_2 \cdot 4H_2O$ (99%, Panreac) powders using a polymer solution method [26,27] in order to assure a high homogeneity in the initial precursor. The powders were weighed in the adequate proportions and dissolved in distilled H_2O, forming a pink clear solution. Polyethyleneimine (PEI) (50% aqueous, Fluka) was added

to the above solution, which turned darker immediately due to the nitrogen-metal bond formation. After partial evaporation (~80 vol.%) of water in a rotary evaporator, the concentrated solution was placed onto a hot plate until a very dark pink paste appeared. Further heating turned this paste to violet color, followed by a slow combustion with the release of brown fumes (nitrogen oxides). The resulting powder was thermally treated twice, at 750 and 800 ºC for 12 h each one, with an intermediate milling, to assure complete carbonate decomposition. This process is of the main importance as it is necessary to avoid carbonates decomposition inside the melt produced on the LFZ process which would lead to the solidification front destabilization. Moreover, some of the released CO_2 could be trapped inside the solid, producing porosity and reducing the samples electrical conductivity.

The calcined powder was then isostatically pressed at 200 MPa in form of cylindrical bars (~ 2-3 mm diameter) which were used as feed and seed in a LFZ device equipped with a continuous power CO_2 laser (Spectron, 200 W, λ = 10.6 μm). The rods were grown downwards using 100 mm h^{-1} pulling rate and rotation rates of 15 and 3 rpm for feed and seed rods in opposite direction, in order to assure a good compositional and thermal homogeneity of the molten zone. After the melt-grown processes, very homogeneous geometrically bars were obtained (~ 2 mm diameter and 60 mm length). On the other hand, the use of the high pulling rate leads to relatively high solidification rate avoiding the formation of $Ca_3Co_4O_9$ phase from the melt. After growing, some samples were kept as reference while others were annealed in air at 900 ºC for 24, 48, 72 and 96 h, with a final furnace cooling, in order to promote the development of

equilibrium phases in these conditions, and decrease the number of the secondary ones, in agreement with the phase diagram represented in Figure 1.

The annealing temperature has been determined using differential thermal analysis (DTA), in a SDT Q600 system (TA Instruments), on the as grown samples at 10 ºC min^{-1} between room temperature and 975 ºC under flowing air.

Phase identification has been performed using powder X-ray diffraction (XRD) utilizing a Rigaku D/max-B X-ray powder diffractometer (CuKα radiation) with 2θ ranging between 10 and 60 degrees, in order to identify the different phases in the as-grown and annealed thermoelectric materials. Microstructural observations were performed on longitudinal polished samples using a Field Emission Scanning Electron Microscope (FESEM, Carl Zeiss Merlin) fitted with an energy dispersive spectrometry (EDS) analysis system.

Apparent density measurements have been performed in all samples after each thermal treatment in order to determine its evolution as a function of the annealing time.

Oxygen content was determined in some of the annealed materials by means of cerimetric titrations. In all cases, 100 ml HCl 1 N were kept under Ar flux during at least 1 h in order to evacuate the oxygen from the reaction vessel, avoiding the reactives oxidation. After this process, 50 mg of the powdered sample was added to the acidic solution to be dissolved, together with 100 mg $FeCl_2$ and a drop of ferroin indicator. In these solutions, Co^{+4} and Co^{+3} are reduced to Co^{+2} while Fe^{+2} is oxidized to Fe^{+3}. The non oxidized Fe^{+2} is then titrated with 0.015 M $Ce(SO_4)_2$ solution, as described elsewhere [27].

Electrical resistivity and thermopower were simultaneously determined by the standard dc four-probe technique in a LSR-3 measurement system (Linseis GmbH). The samples were measured in the steady state mode at temperatures ranging from 50 to 800 ºC under He atmosphere. With the electrical resistivity and thermopower data, PF has been calculated in order to determine the samples performances.

Results and discussion

An image of the typical $Ca_{1-x}Co_xO/Ca_yCo_{1-y}O$ cylindrical rods grown by the LFZ method is shown in Figure 2. These rods were grown from polycrystalline feed and seed rods with $Ca_3Co_4O_9$ nominal composition. The growth processes were performed downwards, in order to avoid bubbles in the solidification front, as they tend to escape to the upper part of the melt. Moreover, the feed rod has been rotated at 15 rpm to assure the melt compositional homogeneity while the seed rod has been rotated in the opposite direction at 3 rpm to maintain the cylindrical geometry. The growth process starts at 1 mm h^{-1} and, when the equilibrium between the melting and solidifying material is reached, it is rapidly increased to 100 mm h^{-1} to produce the cylindrical rods. After the growth process, long (more than 5 cm length) and dimensionally homogeneous rods have been obtained, as illustrated in Figure 2.

Differential thermal analysis (DTA) analysis performed on as-grown materials is displayed in Figure 3, where the evolution of heat flow as a function of temperature, together with its derivative (between 700 and 975 ºC for clarity) are shown. Two well differenced peaks can be observed in the derivative curve: the first one, appearing at around 900 ºC (indicated by #1 in the figure) is

associated with the formation of $Ca_3Co_4O_9$ phase; and the second one at about 960 ºC (#2) represents the development of the $Ca_2Co_3O_6$ one, in agreement with the phase equilibrium diagram (see Figure 1). As a consequence, the annealing temperature to produce the $Ca_3Co_4O_9$ thermoelectric phase formation has been fixed in 900 ºC.

Powder XRD patterns for the as-grown and annealed $Ca_3Co_4O_9$ rods are displayed in Figure 4. From the interpretation of data represented in Figure 4a, it is clear that as-grown samples are composed by a mixture of CaO with $Fm\bar{3}m$ space group [28] and CoO with $Fm\bar{3}m$ space group [29] (peaks identified by their formula). Furthermore, a shift on the CoO peaks to slightly lower angles (around 0.35 degrees), with respect to the reference, can be observed, evidencing the formation of a $Ca_yCo_{1-y}O$ solid solution. On the other hand, no shift is detected for the CaO peaks which indicates that none or very small Ca for Co substitution has been produced. Other interesting feature that can be observed in this diffractogram is that there is no evidence of $Ca_3Co_4O_9$ phase can be found in these samples, as expected according to the phase diagram (see Figure 1). This is a predictable result, as $Ca_3Co_4O_9$ is the equilibrium phase and usually the phases obtained by the LFZ technique are out of equilibrium, considering the low temperature region of the phase diagram. The rapid solidification, characteristic of this technique, hinders the reaction that leads to the formation of low temperature equilibrium phases, favouring the development of the non-equilibrium ones. This phenomenon is particularly critical when seeking to develop phases with incongruent melting.

When annealing processes are performed to the as-grown samples, it can be observed that just after 24 h annealing (Fig. 3b), the $Ca_3Co_4O_9$ phase [30]

(indicated by the diffraction planes in Fig. 3e) is found to be the major one, accompanied by small amounts of CaO, $Ca_yCo_{1-y}O$ and $Ca_3Co_2O_6$ (identified by a * in Fig. 3e) [31]. Further annealing time significantly decreases the amount of secondary phases due to their reaction to produce the equilibrium phase, the $Ca_3Co_4O_9$.

In Figure 5, a representative SEM micrograph performed on longitudinal polished sections of the as-grown samples is displayed. These samples are formed by a divorced eutectic structure in the whole volume, which is composed by a mixture of two solid solutions (identified by EDS): $Ca_{1-x}Co_xO$ (#1, dark grey contrast) immersed in a matrix of $Ca_yCo_{1-y}O$ (#2, light grey contrast). Moreover, the composition of each solid solution, obtained by EDS for guidance purposes, has been performed in several zones and samples, indicating that Ca content in $Ca_yCo_{1-y}O$ ($y = 0.22 \pm 0.03$) is much higher than the Co content in $Ca_{1-x}Co_xO$ ($x = 0.08 \pm 0.02$), in agreement with the XRD results. These results are also in good accordance to the phase equilibrium diagram (see Figure 1). The photomicrography also put in evidence the preferential orientation of the fibre microstructure produced in the laser floating zone technique. This favourable grain alignment is promoted by the high thermal gradients that exist at the solidification interface. On the other hand, the fact that no equilibrium phases can be detected with the XRD or SEM techniques is related to the high solidification rate (100 mm h^{-1}) used in this work which avoids the formation of the equilibrium phase.

Annealing process promotes substantial microstructural changes in a relatively short time, as illustrated by Figure 6, where two micrographs performed on longitudinal polished sections of the 24 h annealed samples in the outer (Figure

6a) and inner (Figure 6b) part of the rods are shown. As it can be clearly seen in Figure 6a (external part of the rods), the major contrast is the grey one (identified by #1), corresponding to the $Ca_3Co_4O_9$ thermoelectric phase, accompanied of small amounts of a darker grey contrast (#2) associated to the $Ca_3Co_2O_6$ phase and some porosity (black contrast). The extent of this transformation has been made by measuring the thickness of this region in several zones of the samples and it has been found that it is about 0.5 mm in depth (for samples with around 2 mm diameter). On the other hand, the inner part of the samples is mainly composed by the divorced eutectic structure explained for the as-grown materials, accompanied by small amounts of the $Ca_3Co_2O_6$ phase (identified by #2 in Figure 6b). The development of this phase is also in agreement with the phase diagram (see Figure 1) since it can be considered as an intermediate stage in the formation of the equilibrium phase, the $Ca_3Co_4O_9$. For 48 h annealing time it is produced the disappearing of the eutectic structure in the whole sample, increasing the amount of $Ca_3Co_4O_9$ and $Ca_3Co_2O_6$ in the inner part while this last phase vanishes from the outer part of the rods. Finally, for higher annealing times, the amount of $Ca_3Co_4O_9$ phase increases while the $Ca_3Co_2O_6$ decreases, leading to very low porosity samples with nearly pure $Ca_3Co_4O_9$ phase, as illustrated in Figure 7. In this micrograph, a representative low magnification image of a longitudinal polished section of the 72 h annealed sample is displayed. In the micrograph it can be seen that only a small amount of porosity is present as small and dark spots, indicating that a high density $Ca_3Co_4O_9$ thermoelectric material is obtained.

The evolution of microstructure and phases content with annealing time can be explained from the oxygen content of different phases. As it can be easily

deduced, the formation of $Ca_3Co_4O_9$ and $Ca_3Co_2O_6$ phases from the $Ca_{1-x}Co_xO/Ca_yCo_{1-y}O$ divorced eutectic structure involves an increase on the total oxygen content in the system. As visible from microstructures, the rods are very dense and oxygen diffusion into the system is relatively slow, which explains the different microstructures and phases found as a function of annealing time. This result is in agreement with the observations made in other very dense ceramic systems where it is necessary to increase the oxygen content to achieve their best electrical properties [32,33]. This process can last around 100 h due to the low diffusion speed of oxygen through the ceramic in the absence of porosity. In order to confirm these observations, apparent density measurements were performed on three samples after each step with an estimated error of about $\pm$ 0.01 g cm^{-3} in all cases, as can be seen in Table I where the measured density and their relative errors are displayed, together with the % of the theoretical density. These measurements have shown that the as grown materials (4.86 g cm^{-3}) possess about 98 % of the calculated theoretical density of the CaO and CoO mixture (~ 4.98 g cm^{-3}). From these values, density decreases with annealing time due to the $Ca_3Co_4O_9$ phase formation, with lower theoretical density (~ 4.68 g cm^{-3}) [34]. The measured values for the 24 and 48 h hours annealed samples (4.77 and 4.71 g cm^{-3}, respectively) are still higher than the $Ca_3Co_4O_9$ theoretical density due to the presence of unreacted secondary phases. As a consequence, no % of the theoretical density has been displayed in Table I, as it is very difficult estimating the amount of each phase in these samples. On the other hand, for samples annealed for 72 and 96 hours, which show nearly $Ca_3Co_4O_9$ pure phase, the obtained values (4.59 and 4.58 g cm^{-3}) are very similar and correspond to around 98 % of the $Ca_3Co_4O_9$ theoretical

density, much higher than the obtained by the classical sintering methods [27,35]. This evolution of density with annealing time confirms the proposed mechanism for the microstructural changes discussed in the SEM observations. Moreover, for samples with nearly $Ca_3Co_4O_9$ single phase (72 and 96 h annealed ones) oxygen analysis has been performed by using cerimetric titration. For each sample three determinations were performed, showing a reproducibility of around ±0.008. The obtained mean values for the average Co valence have been 3.070 and 3.100 for the 72 and 96 h samples, indicating an increase on the oxygen content with the annealing time and reinforcing the above considerations.

Other interesting feature can be observed in Figure 8, where a higher magnification micrograph of a representative image of a longitudinal polished section of the 72 h annealed sample is displayed. In this micrograph it can easily be seen that the $Ca_3Co_4O_9$ grains are randomly oriented, probably due to the nucleation process which occurs at the grain boundaries without any directional restriction, leading to that randomly oriented microstructure.

Electrical resistivity measurements as a function of temperature have been performed on the as-grown and annealed samples, and displayed in Figure 9. In this figure, it is clear that resistivity values decrease when temperature is increased, indicating a semiconducting-like behaviour ($d\rho/dT \leq 0$) in the whole measured temperature range. The as-grown samples values have been displayed in the insert in Figure 9 due to their very high resistivity values, ranging between ~ 9000 and ~ 2000 mΩ.cm at 400 and 800 ºC, respectively. These samples could not be measured at lower temperatures due to their high resistivity values which are higher than the system maximum measuring range.

On the other hand, the obtained resistivity values are in agreement with the XRD results and SEM observations which indicate the absence of thermoelectric phase in the as-grown samples, only composed by $Ca_{1-x}Co_xO$ and $Ca_yCo_{1-y}O$ solid solutions. For the annealed samples, the room temperature resistivity decreases with the annealing time from about 28 mΩ.cm for the 24 h annealed sample to around 15 mΩ.cm for the 96 h one. Moreover, the resistivity evolution with temperature is very similar for all samples, except in the high temperature range for the 72 and 96 h annealed samples which reach the same resistivity values.

The room temperature behaviour of these samples can be easily explained from the XRD data and SEM observations, where the 24 h annealed samples are composed by a mixture of $Ca_3Co_4O_9$, $Ca_3Co_2O_6$, $Ca_yCo_{1-y}O$ and $Ca_{1-x}Co_xO$ in the outer part, and by $Ca_{1-x}Co_xO$ and $Ca_yCo_{1-y}O$, with small amounts of $Ca_3Co_2O_6$ in the inner part. When annealing time is increased, the inner part phases mixture changes and the phases distribution is approximately the same in the whole sample. This effect, together with a reduction on the secondary phases content, lead to a decrease on the room temperature resistivity, compared with the 24 h annealed samples. Further annealing time promotes the formation of a higher amount of $Ca_3Co_4O_9$ phase and, as a consequence, to additional decrease of resistivity. The minimum resistivity values at room temperature, about 15 mΩ.cm for the 96 h annealed samples, are around the best values obtained on textured samples produced by SPS (between 14 and 18 mΩ.cm) [36]. This very low values outcome not only by the high amount of $Ca_3Co_4O_9$ phase, but also by the very high density values obtained in these samples and discussed previously.

Figure 10 shows the variation of the Seebeck coefficient with the temperature for the as-grown and annealed samples. It can be clearly seen that the sign of the thermopower is positive for the entire measured temperature range, which confirms a conduction mechanism predominantly governed by holes. The values of the thermopower increase with temperature, with the same behaviour for all the annealed samples. For the as-grown ones (see insert in Fig. 8), only the 400-800 ºC temperature range has been measured, as explained for the resistivity measurements. The Seebeck coefficient measured in these samples increases very rapidly, from ~ 80 to about 550 $\mu V\ K^{-1}$, for 400 and 800 ºC, respectively. These values are very high and agree with the high resistivity values measured and explained previously. When considering the annealed samples, they increase Seebeck coefficient values, at room temperature, with the annealing time, except for the 96 h annealed sample which is decreasing with respect to the 72 h one. The raise in S with annealing time, from 24 to 72 h, can be explained from the higher proportion of $Ca_3Co_4O_9$ when the annealing process is longer. In order to explain the decrease on S for the 96 h annealed sample, it is necessary to make some considerations. Firstly, all the measured S values at room temperature are much higher than the usual ones reported in the literature for textured materials (~120 $\mu V\ K^{-1}$ at 275 ºC) [21]. Secondly, as it is well known, Koshibae's expression [37], which relates S value to the fraction of Co^{+4} over the total amount of cobalt, describes the behaviour of most of the Co-based thermoelectric materials at room temperature. On the other hand, in the $Ca_3Co_4O_9$ case, it has been demonstrated that they are not really described by that expression even if they follow the same trends: lower Co^{+4} amount leads to higher S values [27,38]. Moreover, the lower Co^{+4} amounts can be

associated with lower oxygen content in the samples. From all these considerations, it is possible to deduce that 96 h annealed samples possess higher amount of oxygen (and Co^{+4} contents) than the 72 h annealed ones explaining the Seebeck difference at room temperature, in agreement with the oxygen contents found in the titrations described previously.

With the electrical resistivity and Seebeck factor values, PF variation with temperature has been calculated and represented in Figure 11. As observed previously, PF values for the as-grown materials (represented in insert in Figure 11) are very small due to the high resistivity measured in these samples. In the case of annealed samples, it can be clearly seen that room temperature values increase from ~ 0.09 mW K^{-2} m^{-1} for the 24 h annealed samples, to ~ 0.11 mW K^{-2} m^{-1} for the 48 h one, and ~ 0.17 mW K^{-2} m^{-1}.m for higher annealing times. The maximum value at 800 ºC (~ 0.42 mW K^{-2} m^{-1}) obtained for samples annealed for 72 h, is around those measured on textured materials produced by one of the newest texturing methods used in the $Ca_3Co_4O_9$ system, the spark plasma texturing (SPT) technique (~ 0.40 mW K^{-2} m^{-1} at 550 ºC) [39]. These high PF values make these melt-grown annealed materials promising candidates for practical applications in thermoelectric devices.

Conclusions

This work demonstrates that high-performance $Ca_3Co_4O_9$ thermoelectric materials can be produced by a new two-step process involving the LFZ growth of a very fine $Ca_{1-x}Co_xO/Ca_yCo_{1-y}O$ divorced eutectic structure, followed by an annealing process at 900 ºC. It has been found that the reaction between $Ca_{1-x}Co_xO$ and $Ca_yCo_{1-y}O$ to produce the $Ca_3Co_4O_9$ phase starts in the outer part of

the rods and continues to the central part of the rods due to the relatively low oxygen diffusion rate through the high-density ceramic material.

The optimal annealing time has been determined using the values of the power factor at 800 ºC, which is maximum for the 72 h annealed samples with values around 0.42 mW K^{-2} m^{-1} (about 100 % higher than the obtained for the 24 and 48 h annealed ones). These high PF values have been obtained from the decrease on the electrical resistivity associated to the high density and amount of $Ca_3Co_4O_9$ phase in the 72 and 96 h annealed samples, together with an increase on the Seebeck coefficient due to the slow oxygen diffusion to the inner part of the samples.

All these results make this laser melt-grown $Ca_{1-x}Co_xO/Ca_yCo_{1-y}O$ divorced eutectic structure a promising precursor for $Ca_3Co_4O_9$ ceramics with high thermoelectric performances for practical power generation applications.

Acknowledgements

The work was supported by the cooperation projects: E-41/11 and AIB2010-PT-00247.

The authors wish to thank the Gobierno de Aragón (Research Groups T12 and T87), the Spanish Ministry for Science and Innovation-FEDER (Project MAT2008-00429), and the Universidad de Zaragoza (Project UZ2011-TEC-03) for financial support. The technical contributions of L. C. Estepa and C. Gallego are also acknowledged. Sh. Rasekh acknowledges a JAE-PreDoc2010 grant from CSIC.

Funding by PEst-C/CTM/LA0025/2011 is gratefully acknowledged.

References

1. Rowe DM, editor. *Thermoelectrics handbook: macro to nano*. 1st ed. Boca Raton, FL: CRC Press; 2006. p. 1-3–1-7.

2. Mahan G, Sales B, Sharp J. Thermoelectric materials: New approaches to an old problem. *Phys Today* 1997;**50**:42–7.

3. Naito H, Kohsaka Y, Cooke D, Arashi H. Development of a solar receiver for a high-efficiency thermionic/thermoelectric conversion system. *Sol Energy* 1996;**58**:191–5.

4. Kim CM, Hwang YJ, Ryu YH. US Patent US6393842. May, 2002.

5. Terasaki I, Sasago Y, Uchinokura K. Large thermoelectric power in $NaCo_2O_4$ single crystals. *Phys Rev B* 1997;**56**:12685–7.

6. Funahashi R, Matsubara I, Ikuta H, Takeuchi T, Mizutani U, Sodeoka S. An oxide single crystal with high thermoelectric performance in air. *Jpn J Appl Phys* 2000;**39**:L1127–9.

7. Masset AC, Michel C, Maignan A, Hervieu M, Toulemonde O, Studer F, Raveau B, Hejtmanek. Misfit-layered cobaltite with an anisotropic giant magnetoresistance: $Ca_3Co_4O_9$. *Phys Rev B* 2000;**62**:166–75.

8. Leligny H, Grebille D, Perez O, Masset AC, Hervieu M, Raveau B. A five-dimensional structural investigation of the misfit layer compound $[Bi_{0.87}SrO_2]_2[CoO_2]_{1.82}$. *Acta Cryst B* 2000;**56**:173–82.

9. Maignan A, Pelloquin D, Hébert S, Klein Y, Hervieu M. Thermoelectric power in misfit cobaltites ceramics: optimization by chemical substitutions. *Bol Soc Esp Ceram V* 2006;**45**:122–5.

10. Maignan A, Hébert S, Hervieu M, Michel C, Pelloquin D, Khomskii D. Magnetoresistance and magnetothermopower properties of Bi/Ca/Co/O and

Bi(Pb)/Ca/Co/O misfit layer cobaltites. *J Phys: Condens Matter* 2003;**15**:2711–23.

11. Sotelo A, Guilmeau E, Rasekh Sh, Madre MA, Marinel S, Diez JC. Enhancement of the thermoelectric properties of directionally grown Bi-Ca-Co-O through Pb for Bi substitution. *J Eur Ceram Soc* 2010;**30**:1815–20.

12. Tanaka Y, Fujii T, Nakanishi M, Kusano Y, Hashimoto H, Ikeda Y, Takada, J. Systematic study on synthesis and structural, electrical transport and magnetic properties of Pb-substituted Bi-Ca-Co-O misfit-layer cobaltites . *Solid State Commun* 2007;**141**:122–6.

13. Liu HQ, Zhao XB, Zhu TJ, Song Y, Wang FP. Thermoelectric properties of Gd, Y co-doped $Ca_3Co_4O_{9+\delta}$. *Current Appl Phys* 2009;**9**:409–13.

14. Shin W, Murayama N. Thermoelectric properties of (Bi,Pb)-Sr-Co-O oxide. *J Mater Res* 2000;**15**:382–6.

15. Sotelo A, Rasekh Sh, Guilmeau E, Madre MA, Torres MA, Marinel S, Diez JC. Improved thermoelectric properties in directionally grown $Bi_2Sr_2Co_{1.8}O_y$ ceramics by Pb for Bi substitution. *Mater Res Bull* 2011;**46**:2537–42.

16. Sotelo A, Torres MA, Constantinescu G, Rasekh Sh, Diez JC, Madre MA. Effect of Ag addition on the mechanical and thermoelectric performances of annealed $Bi_2Sr_2Co_{1.8}O_x$ textured ceramics. *J Eur Ceram Soc* 2012;**32**:3745–51.

17. Sotelo A, Rasekh Sh, Constantinescu G, Torres MA, Madre MA, Diez JC. Improvement of textured $Bi_{1.6}Pb_{0.4}Sr_2Co_{1.8}O_x$ thermoelectric performances by metallic Ag additions. *Ceram Int* 2013;**39**:1597–602

18. Zhang Y, Zhang J, Lu Q. Synthesis of highly textured $Ca_3Co_4O_9$ ceramics by spark plasma sintering. *Ceram Int* 2007;**33**:1305–8.

19. Noudem JG, Kenfaui D, Chateigner D, Gomina M. Granular and Lamellar Thermoelectric Oxides Consolidated by Spark Plasma Sintering. *J Electronic Mater* 2011;**40**:1100–6.

20. Prevel M, Perez O, Noudem JG. Bulk textured $Ca_{2.5}(RE)_{0.5}Co_4O_9$ (RE: Pr, Nd, Eu, Dy and Yb) thermoelectric oxides by sinter-forging. *Solid State Sci* 2007;**9**:231–5.

21. Itahara H, Xia C, Sugiyama J, Tani T. Fabrication of textured thermoelectric layered cobaltites with various rock salt-type layers by using *b*-$Co(OH)_2$ platelets as reactive templates. *J Mater Chem* 2004;**14**:61–6.

22. Sotelo A, Guilmeau E, Madre MA, Marinel S, Diez JC, Prevel M. Fabrication and properties of textured Bi-based cobaltite thermoelectric rods by zone melting. *J Eur Ceram Soc* 2007;**27**:3697–700.

23. Ferreira NM, Rasekh Sh, Costa FM, Madre MA, Sotelo A, Diez JC, Torres MA. New method to improve the grain alignment and performance of thermoelectric ceramics. *Mater Lett* 2012;**83**:144–7.

24. Sotelo A, Mora M, Madre MA, Diez JC, Angurel LA, de la Fuente GF. Ag distribution in thick Bi-2212 floating zone textured rods. *J Eur Ceram Soc* 2005;**25**:2947–50.

25. Sedmidubský D, Jakes V, Jankovský O, Leitner J, Sofer Z, Hejtmánek J. Phase equilibria in Ca–Co–O system. *J Solid State Chem* 2012;**194**:199–205.

26. Sotelo A, Rasekh Sh, Madre MA, Guilmeau E, Marinel S, Diez JC. Solution-based synthesis routes to thermoelectric $Bi_2Ca_2Co_{1.7}O_x$. *J Eur Ceram Soc* 2011;**31**:1763–9.

27. Sotelo A, Constantinescu G, Rasekh Sh, Torres MA, Diez JC, Madre MA. Improvement of thermoelectric properties of $Ca_3Co_4O_9$ using soft chemistry synthetic methods. *J Eur Ceram Soc* 2012;**32**:2415–22.

28. Ghebouli MA, Ghebouli B, Bouhemadou A, Fatmi M, Bouamama K. Structural, electronic, optical and thermodynamic properties of $Sr_xCa_{1-x}O$, $Ba_xSr_{1-x}O$ and $Ba_xCa_{1-x}O$ alloys. *J Alloys Compd* 2011;**509**:1440–7.

29. Liu J-F, Yin S, Wu H-P, Zeng YW, Hu XR, Wang YW, Lv GL, Jiang J-Z. Wurtzite-to-rocksalt structural transformation in nanocrystalline CoO. *J Phys Chem B* 2006;**110**:21588–92.

30. JCPDS 21-0139

31. JCPDS 23-0111

32. Marinel S, Bourgault D, Belmont O, Sotelo A, Desgardin G. Microstructure and transport properties of YBCO zone melted samples processed in a microwave cavity and infra-red furnace. *Physica C* 1999;**315**:205–14.

33. Meslin S, Iida K, Babu N Hari, Cardwell DA, Noudem JG. The effect of Y-211 precursor particle size on the microstructure and properties of Y-Ba-Cu-O bulk superconductors fabricated by seeded infiltration and growth. *Supercond Sci Technol* 2006;**19**:711–8.

34. Liou YC, Tsai WC, Lin WY, Lee UR. Synthesis of $Ca_3Co_4O_9$ and $CuAlO_2$ Ceramics of the Thermoelectric Application Using A Reaction- Sintering Process. *J Aust Ceram Soc* 2008;**44**:17–22.

35. Diez JC, Torres MA, Rasekh Sh, Constantinescu G, Madre MA, Sotelo A. Enhancement of $Ca_3Co_4O_9$ thermoelectric properties by Cr for Co substitution. *Ceram Int* (2013) DOI: 10.1016/j.ceramint.2013.01.021

36. Kenfaui D, Bonnefont G, Chateigner D, Fantozzi G, Gomina M, Noudem JG. $Ca_3Co_4O_9$ ceramics consolidated by SPS process: optimisation of mechanical and thermoelectric properties. *Mater Res Bull* 2010;**45**:1240–9.

37. Koshibae W, Tsuitsui K, Maekawa S. Thermopower in cobalt oxides. *Phys Rev B* 2000;**62**:6869–72.

38. Karppinen M, Fjellvåg H, Konno T, Morita Y, Motohashi T, Yamauchi H. Evidence for oxygen vacancies in misfit-layered calcium cobalt oxide, [CoCaO]CoO. *Chem Mater* 2004;**16**:2790–3.

39. Noudem JG, Kenfaui D, Chateigner D, Gomina M. Toward the enhancement of thermoelectric properties of lamellar $Ca_3Co_4O_9$ by edge-free spark plasma texturing. *Scripta Mater* 2012;**66**:258–60.

Table I. Measured density values for all samples, together with their standard error and the % of the theoretical density.

Thermal treatment	Density (gr/cm^3)	Standard error	% theoretical density
As-grown	4.86	0.01	98
24 h 900 ºC	4.77	0.01	----
48 h 900 ºC	4.71	0.01	----
72 h 900 ºC	4.59	0.01	98
96 h 900 ºC	4.58	0.01	98

Figure captions

Figure 1. Ca-Co-O phase diagram under air atmosphere, adapted from the work of Sedmdubsky *et al.* [25].

Figure 2. Image of an as-grown cylinder produced by the LFZ technique at 100 mm h^{-1} from a polycrystalline precursor with $Ca_3Co_4O_9$ nominal composition.

Figure 3. Heat flow and derivative of heat flow with temperature variation with respect to temperature. The two identified peaks correspond to the formation of 1) $Ca_3Co_4O_9$ phase; and 2) $Ca_3Co_2O_6$ one.

Figure 4. Powder X-ray diffraction patterns obtained for the produced cylindrical rods with nominal $Ca_3Co_4O_9$ composition; (a) as-grown; and annealed at 900 ºC for (b) 24; (c) 48; (d) 72; and (e) 96 h. The reflection planes are indicated on the peaks corresponding to the $Ca_3Co_4O_9$ phase. * indicates the $Ca_3Co_2O_6$ phase and CoO and CaO reflections are indicated by their formula.

Figure 5. Representative SEM micrograph performed on longitudinal polished sections of the as-grown samples which are formed by a divorced eutectic structure composed by: 1) $Ca_{1-x}Co_xO$; and 2) $Ca_yCo_{1-y}O$.

Figure 6. Representative SEM micrographs performed on longitudinal polished sections of the 24 h annealed samples at 900 ºC in the outer (a) and inner (b) part of the rods. The identified phases are 1) $Ca_3Co_4O_9$; and 2) $Ca_3Co_2O_6$. Most

of the internal part is formed by the $Ca_{1-x}Co_xO/Ca_yCo_{1-y}O$ divorced eutectic structure.

Figure 7. Representative low magnification SEM micrograph of a polished section of the 72 h annealed sample where it can be observed the small amount of porosity (black spots) and the high homogeneity of these samples.

Figure 8. Representative SEM micrograph of a polished section of the 72 h annealed sample where it can be observed the random orientation of $Ca_3Co_4O_9$ thermoelectric grains.

Figure 9. Temperature dependence of the electrical resistivity as a function of the annealing time for the $Ca_3Co_4O_9$ samples, (●) 24; (◆) 48; (■) 72; and (▲) 96 h. The insert represents the obtained values for the as-grown samples.

Figure 10. Temperature dependence of the Seebeck coefficient as a function of the annealing time for the $Ca_3Co_4O_9$ samples, (●) 24; (◆) 48; (■) 72; and (▲) 96 h. The insert represents the obtained values for the as-grown samples.

Figure 11. Temperature dependence of the power factor as a function of the annealing time for the $Ca_3Co_4O_9$ samples, (●) 24; (◆) 48; (■) 72; and (▲) 96 h. The insert represents the obtained values for the as-grown samples.

Figure 1

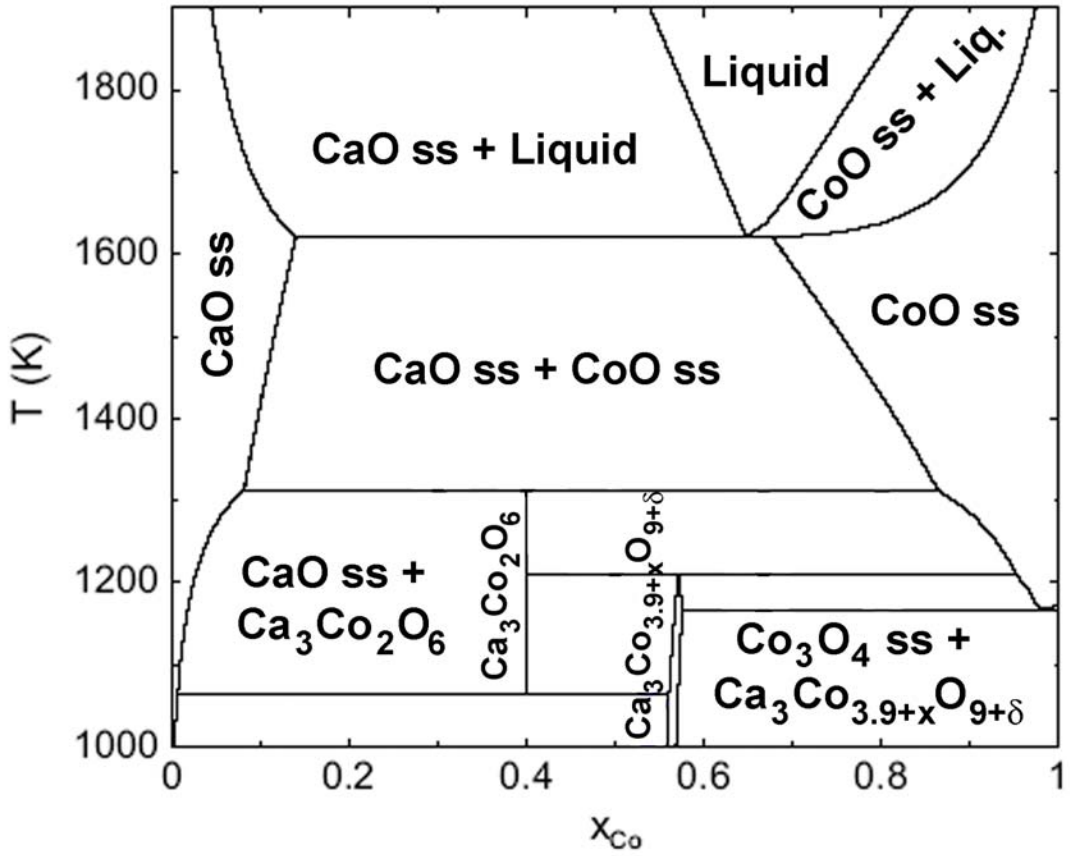
Liquid
CoO ss + Liq.
CaO ss + Liquid
CaO ss
CoO ss
CaO ss + CoO ss
CaO ss +
Ca3Co2O6
Ca3Co2O6
Ca3Co3.9+xO9+δ
Co3O4 ss +
Ca3Co3.9+xO9+δ
T (K)
1800
1600
1400
1200
1000
0
0.2
0.4
0.6
0.8
1
xCo

Figure 2

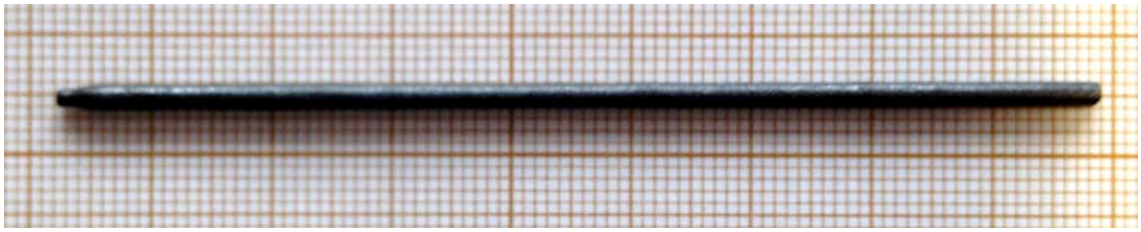

Figure 3

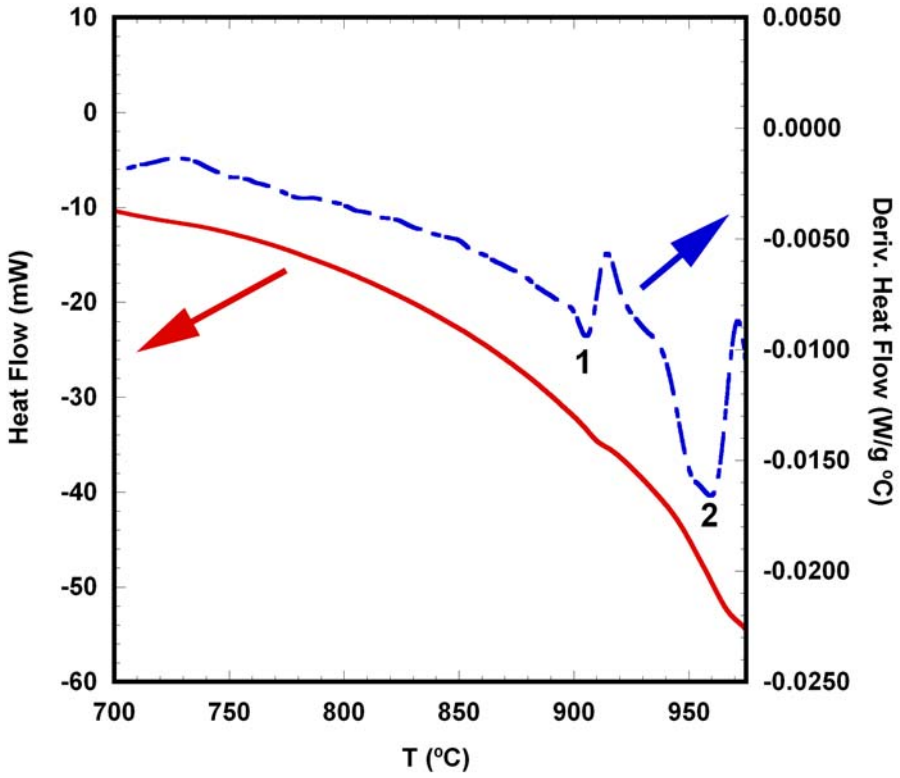
10
0
-10
-20
-30
-40
-50
-60
Heat Flow (mW)
0.0050
0.0000
-0.0050
-0.0100
-0.0150
-0.0200
-0.0250
Deriv. Heat Flow (W/g °C)
700
750
800
850
900
950
T (°C)
1
2

Figure 4

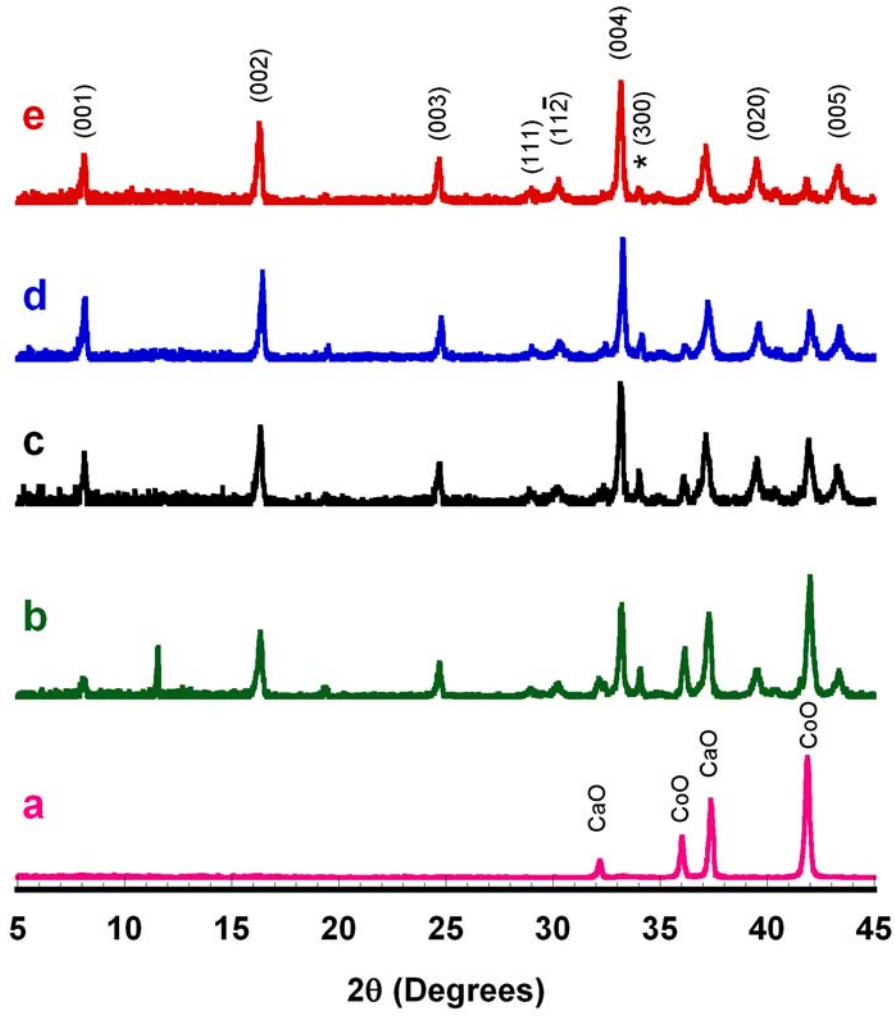
e
d
c
b
a
(001)
(002)
(003)
(111)
(11$\bar{2}$)
(004)
* (300)
(020)
(005)
CaO
CoO
CaO
CoO
5
10
15
20
25
30
35
40
45
2θ (Degrees)

Figure 5

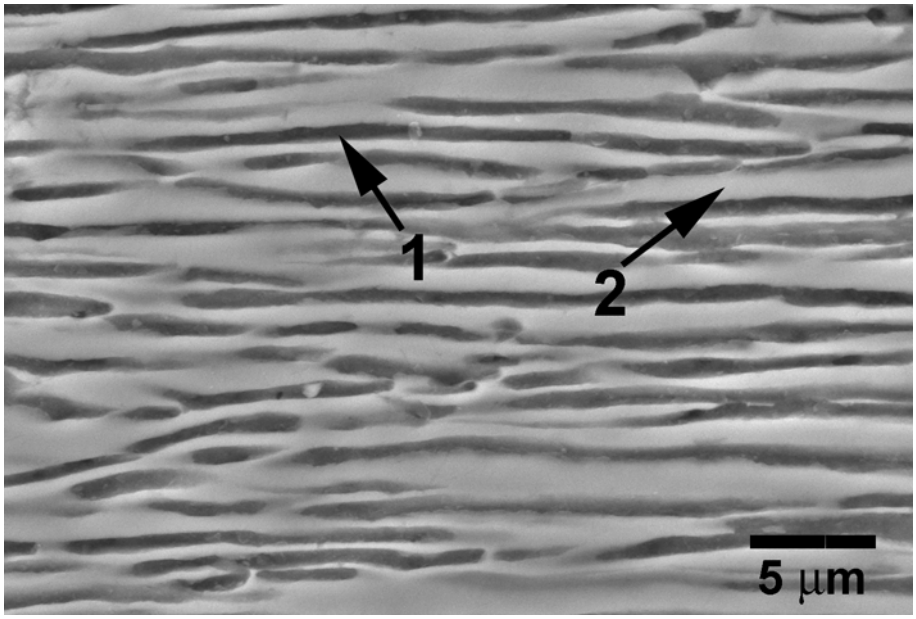

Figure 6

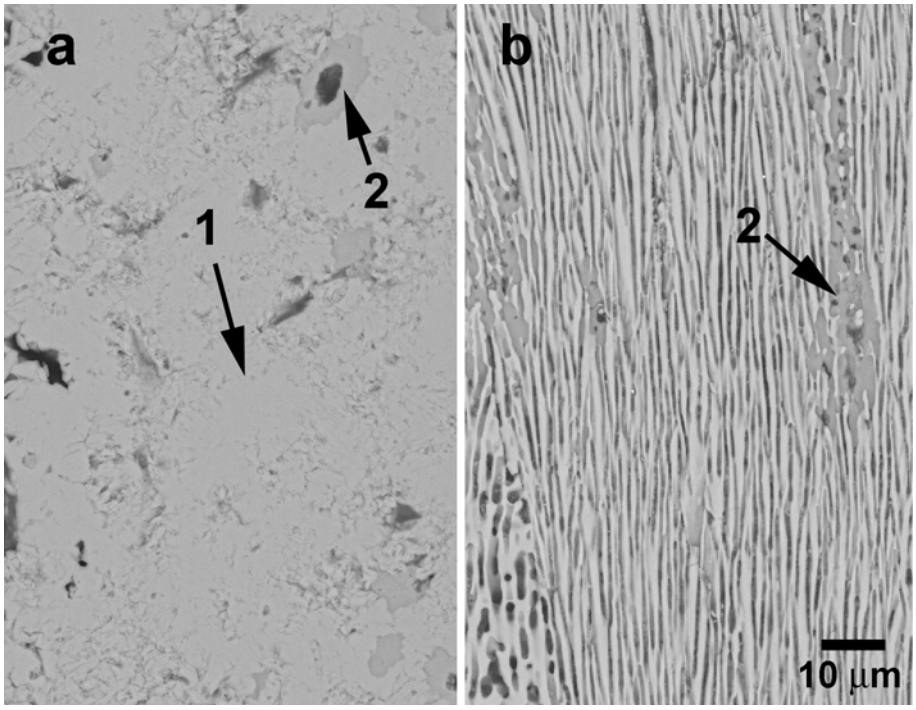

Figure 7

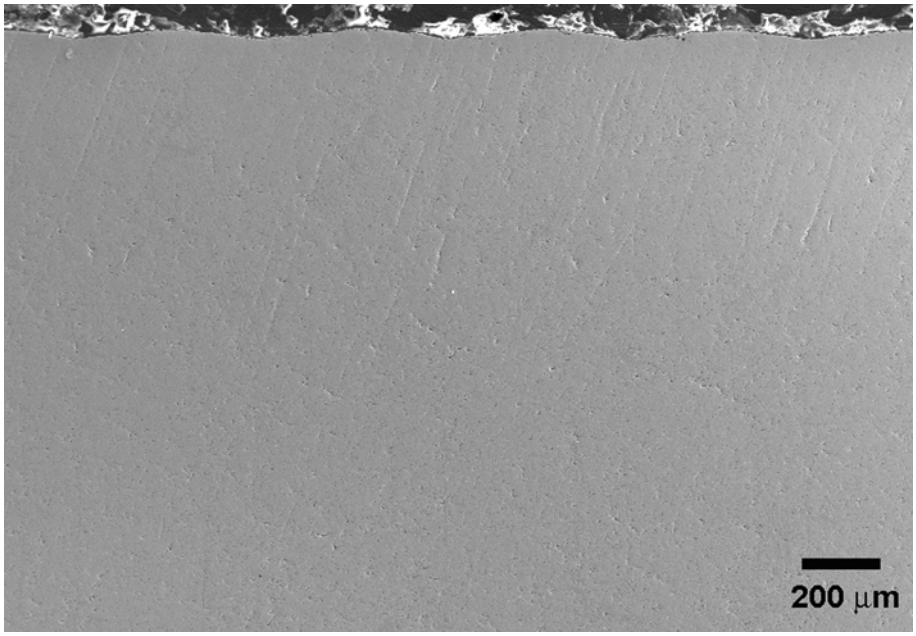

Figure 8

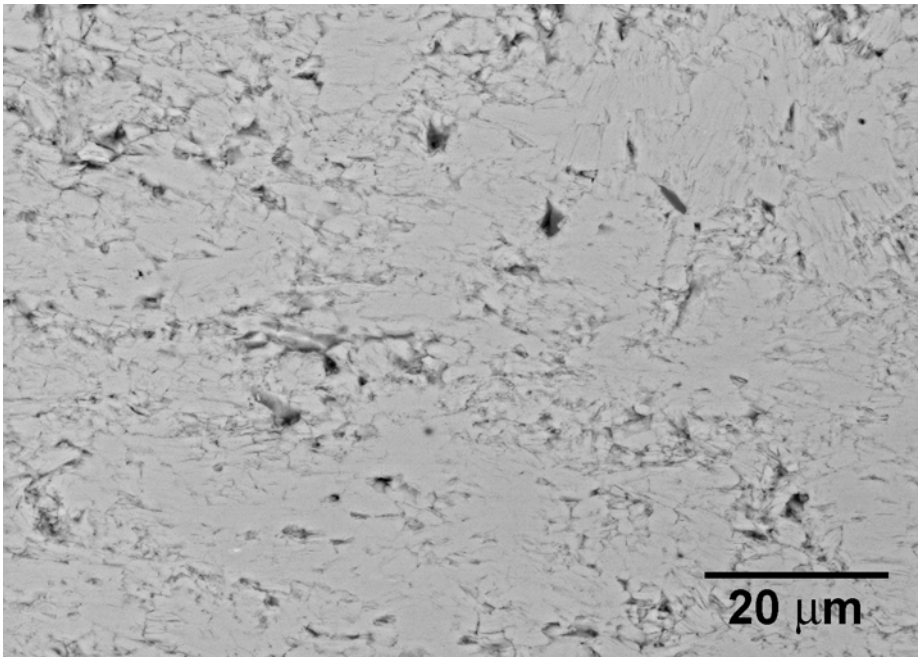

Figure 9

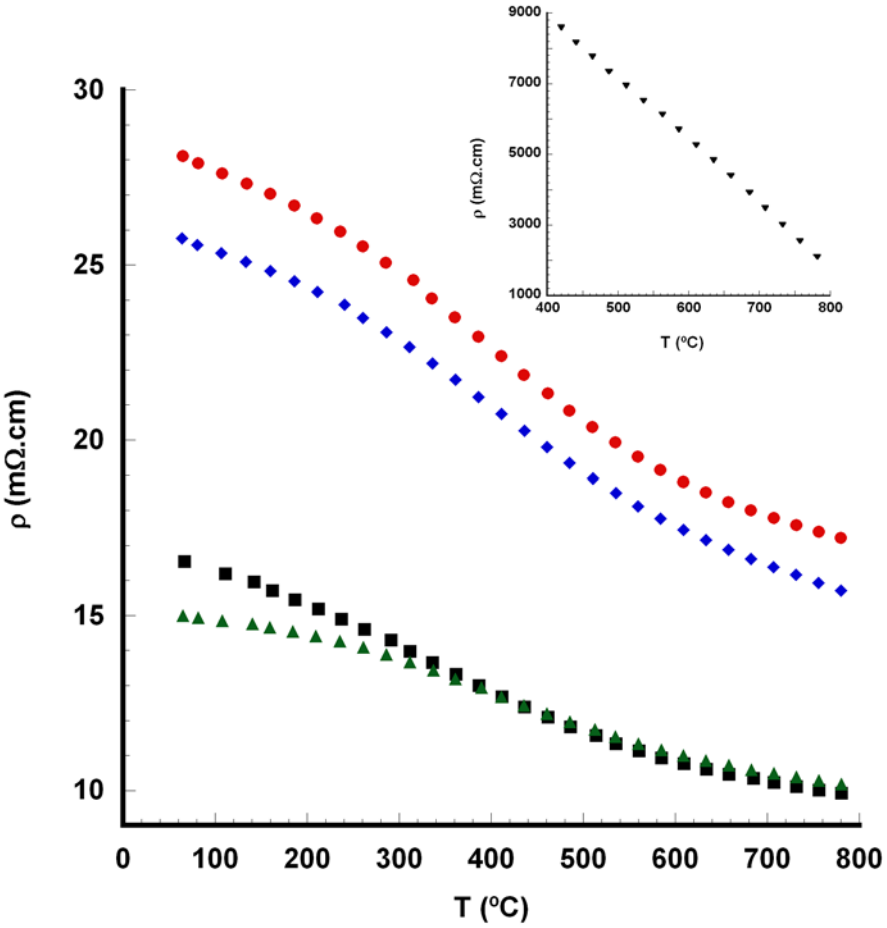
ρ (mΩ.cm)
T (°C)
30
25
20
15
10
0
100
200
300
400
500
600
700
800
9000
7000
5000
3000
1000
400
500
600
700
800
ρ (mΩ.cm)
T (°C)

Figure 10

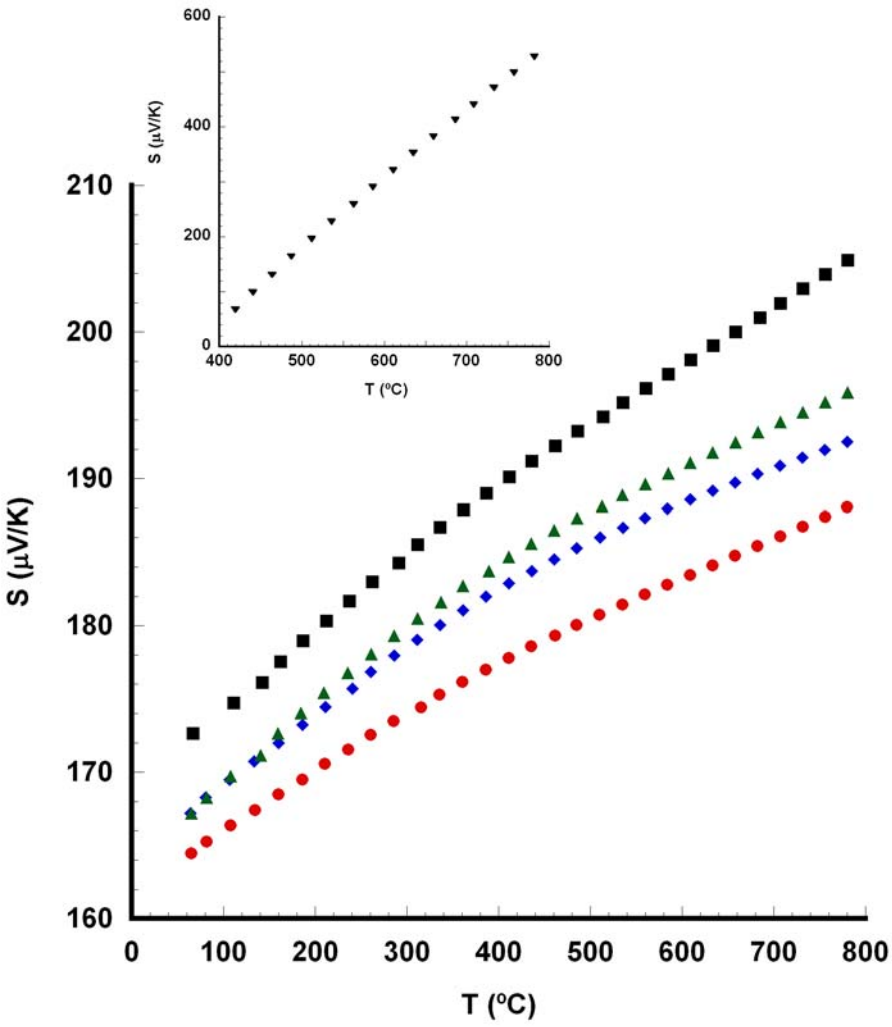
S (μV/K)
T (°C)
160
170
180
190
200
210
0
100
200
300
400
500
600
700
800
S (μV/K)
T (°C)
0
200
400
600
400
500
600
700
800

Figure 11

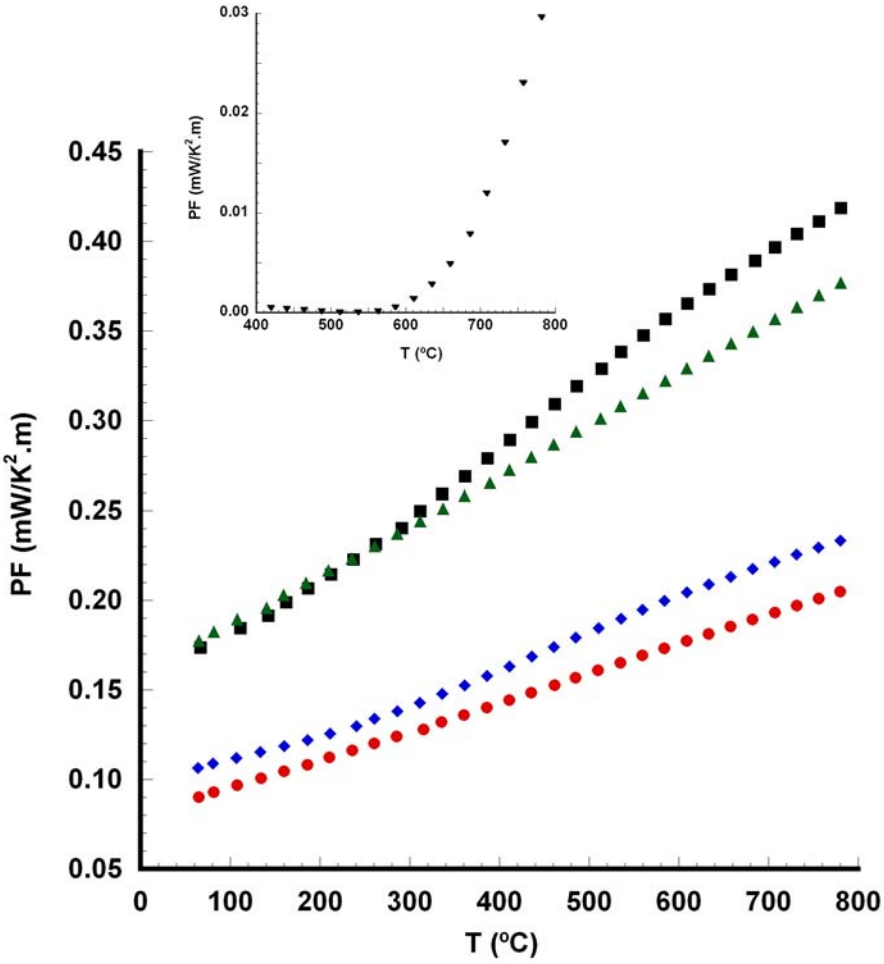
PF (mW/K^2.m)
T (°C)
0.45
0.40
0.35
0.30
0.25
0.20
0.15
0.10
0.05
0
100
200
300
400
500
600
700
800
0.03
0.02
0.01
0.00
400
500
600
700
800